

# Air-Stable Monolayer Cu<sub>2</sub>Se Exhibits a Purely Thermal Structural Phase Transition

Kai Qian, Lei Gao, Xiya Chen, Hang Li, Shuai Zhang, Xian-Li Zhang, Shiyu Zhu, Jiahao Yan, Deliang Bao, Lu Cao, Jin-An Shi, Jianchen Lu, Chen Liu, Jiaou Wang, Tian Qian, Hong Ding, Lin Gu, Wu Zhou, Yu-Yang Zhang, Xiao Lin,\* Shixuan Du,\* Min Ouyang, Sokrates T. Pantelides, and Hong-Jun Gao\*

Materials possessing structural phase transformations exhibit a rich set of physical and chemical properties that can be used for a variety of applications. In 2D materials, structural transformations have so far been induced by strain, lasers, electron injection, electron/ion beams, thermal loss of stoichiometry, and chemical treatments or by a combination of such approaches and annealing. However, stoichiometry-preserving, purely thermal, reversible phase transitions, which are fundamental in physics and can be easily induced, have not been observed. Here, the fabrication of monolayer Cu<sub>2</sub>Se, a new 2D material is reported, demonstrating the existence of a purely thermal structural phase transition. Scanning tunneling microscopy, scanning transmission electron microscopy, and density functional theory (DFT) identify two structural phases at 78 and 300 K. DFT calculations trace the phase-transition mechanism via the existence/absence of imaginary (unstable) phonon modes at low and high temperatures. In situ, variable-temperature low-energy electron diffraction patterns demonstrate that the phase transition occurs across the whole sample at ≈147 K. Angle-resolved photoemission spectra and DFT calculations show that a degeneracy at the  $\Gamma$  point of the energy bands of the high-temperature phase is lifted in the low-temperature phase. This work opens up possibilities for studying such phase transitions in 2D materials.

properties anchor novel device concepts and offer promise for applications.<sup>[1–3]</sup> Structural phase transformations of 2D materials driven by external means have been studied extensively.<sup>[4–18]</sup> For example, electron doping by alloying or intercalation and electron injection trigger phase transformations in MoS<sub>2</sub> and MoTe<sub>2</sub> monolayers.<sup>[6–9]</sup> Thermal treatment, which is the most common method to drive phase transitions in bulk materials, induces phase transformations in VS<sub>2</sub>, VSe<sub>2</sub>, and PtSe<sub>2</sub> monolayers via loss of chalcogen atoms so that reversals require fresh supplies.<sup>[10,15,18]</sup>

Stoichiometry-preserving, purely thermal, reversible structural phase transitions were studied by both experiments and theory more than 20 years ago in self-assembled monolayers of rare-gas atoms and small molecules.<sup>[19]</sup> Such monolayers are held together by weak in-plane van der Waals interactions, in contrast to bona fide 2D materials, which are held together by in-plane chemical bonds. Purely thermal phase transitions in chemically bonded 2D materials, governed by chemical-bond

The advent of monolayer graphene in 2004 as a prototype 2D material led to broad experimental and theoretical investigations of hundreds of 2D materials whose unique and unusual

rearrangements, have been theoretically predicted but have not been observed in any of the 2D materials that have been investigated in the last 15 years.<sup>[20,21]</sup>

Dr. K. Qian, Dr. L. Gao, X. Y. Chen, H. Li, S. Zhang, X.-L. Zhang, Dr. S.-Y. Zhu, Dr. J.-H. Yan, Dr. D.-L. Bao, L. Cao, J.-A. Shi, Dr. J.-C. Lu, Prof. T. Qian, Prof. H. Ding, Prof. L. Gu, Prof. W. Zhou, Prof. Y.-Y. Zhang, Prof. X. Lin, Prof. S.-X. Du, Prof. S. T. Pantelides, Prof. H.-J. Gao  
Institute of Physics and University of Chinese Academy of Sciences  
Chinese Academy of Sciences  
Beijing 100190, P. R. China  
E-mail: xlin@ucas.ac.cn; sxdu@iphy.ac.cn; hjgao@iphy.ac.cn

Dr. D. L. Bao, Prof. S. T. Pantelides  
Department of Physics and Astronomy and Department of Electrical Engineering and Computer Science  
Vanderbilt University  
Nashville, TN 37235, USA

 The ORCID identification number(s) for the author(s) of this article can be found under <https://doi.org/10.1002/adma.201908314>.

Dr. J.-C. Lu  
Faculty of Materials Science and Engineering  
Kunming University of Science and Technology  
Kunming, Yunnan 650000, China

C. Liu, Prof. J. O. Wang  
Institute of High Energy Physics  
Chinese Academy of Sciences  
Beijing 100049, China

Prof. T. Qian, Prof. H. Ding, Prof. W. Zhou, Prof. Y.-Y. Zhang, Prof. X. Lin, Prof. S.-X. Du, Prof. H.-J. Gao  
CAS Center for Excellence in Topological Quantum Computation  
Chinese Academy of Sciences  
Beijing 100190, China

Prof. M. Ouyang  
Department of Physics  
University of Maryland  
College Park, MD 20742-4111, USA

DOI: 10.1002/adma.201908314

Herein, we report a purely thermal structural phase transition in a new 2D material, monolayer  $\text{Cu}_2\text{Se}$ . We fabricated large-scale, high-quality epitaxial monolayer  $\text{Cu}_2\text{Se}$  on bilayer graphene and observed two distinct structures at 300 and 78 K, respectively, using scanning tunneling microscopy (STM). Cross-sectional scanning transmission electron microscopy (STEM) images confirm the material's monolayer form. In situ, low-energy electron diffraction patterns were measured at a continuous temperature ranging from 78 to 300 K. We found that the phase transition occurs across the whole sample at  $\approx 147$  K. The phases below and above 147 K are named  $\zeta$  and  $\lambda$  phases for their zigzag and linear Cu arrangements, respectively. Density functional theory (DFT) calculations are used in conjunction with STM and STEM data to identify the structures and determine their space groups as  $P2_1/c$  and  $P\bar{3}m1$  for the  $\zeta$  and  $\lambda$  phases, respectively. DFT calculations find that the  $\lambda$  phase exhibits imaginary-frequency phonons at 0 K, i.e., the phase is unstable, and the corresponding atomic displacements are precisely what is necessary to drive the system to the  $\zeta$  phase. On the other hand, the  $\lambda$  phase has no imaginary-frequency phonons at 300 K, i.e., it is stable. Finite-temperature quantum molecular dynamics simulations further confirm that the phase transitions are purely thermal. Angle-resolved photoemission spectroscopy (ARPES) and calculated energy bands find that a band splitting occurs at the  $\Gamma$  point near the Fermi level as the  $\text{Cu}_2\text{Se}$  monolayer undergoes a  $\lambda$ -to- $\zeta$  phase transition. The present demonstration of a purely thermal, reversible, structural phase transition in a monolayer material provides a new platform for future investigations.

The sample is prepared by direct coevaporation of Se and Cu onto bilayer graphene (BLG) (see the Supporting Information for more details). X-ray photoelectron spectroscopy (XPS) data reveal that the composition of the sample is  $\text{Cu}_2\text{Se}$  (Figure S1, Supporting Information).<sup>[22]</sup> A large-scale STM image is shown in Figure S2a (Supporting Information). A zoomed-in STM image (Figure 1a) taken at liquid-nitrogen temperature (78 K) shows 1D stripes. An atomic-resolution STM image (Figure 1b) and its fast Fourier transform (FFT) (Figure 1c) show that the film possesses a rectangular unit cell, with a lattice constant of  $a = 0.42 \pm 0.05$  nm and  $b = 0.71 \pm 0.05$  nm.

Based on the STM images and previously reported predictions for bulk layered  $\text{Cu}_2\text{Se}$ , we constructed the atomic model shown in Figure 1d.<sup>[23,24]</sup> This  $\zeta$ -phase structure is the basic layer in bulk layered  $\text{Cu}_2\text{Se}$  and has the space group  $P2_1/c$ .<sup>[23,24]</sup> The DFT-relaxed lattice constants,  $a = 0.41$  nm and  $b = 0.67$  nm, agree with the measured values  $a = 0.42 \pm 0.05$  nm and  $b = 0.71 \pm 0.05$  nm. The atomic model and corresponding simulated STM image are overlaid in Figure 1b, demonstrating that the bright spots in the STM image are top-layer Se atoms. The excellent agreement between the simulated and experimental images confirm a  $\zeta$ -phase  $\text{Cu}_2\text{Se}$ . Considering the BLG substrate, a  $(1 \times 14)$   $\text{Cu}_2\text{Se}$  sitting on a  $(3 \times 15\sqrt{3})$  BLG model is proposed. The 1D moiré pattern shown in Figure 1a is perfectly reproduced (Figure S3, Supporting Information).

In Figure 1e,f, we show STM images at 300 K, revealing no 1D moiré pattern. We deduced the structure of the new phase using atomic-resolution STM and STEM images (Figures 1f and 2a, respectively) and the corresponding FFTs (Figures 1g and 2b, respectively), finding a hexagonal lattice with a higher

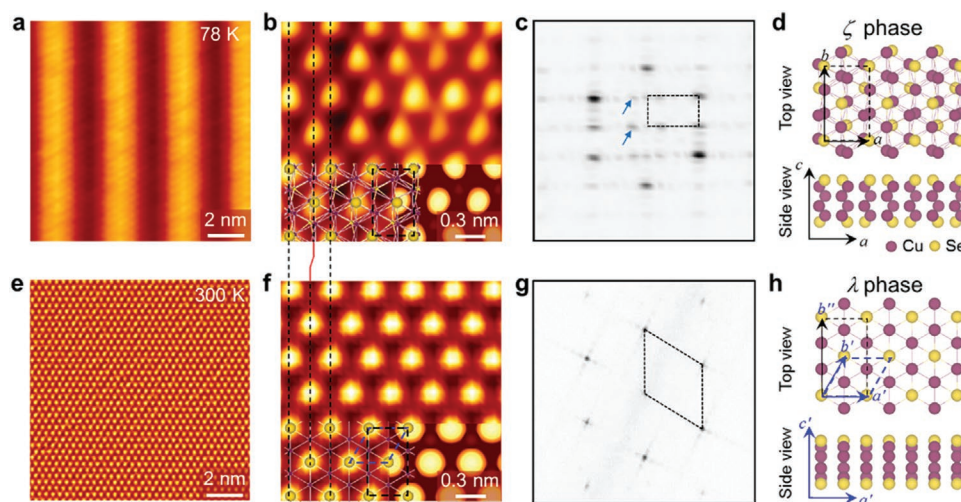


**Figure 1.** STM images and atomic configurations of monolayer  $\text{Cu}_2\text{Se}$  at 78 and 300 K. a) An STM image of  $\text{Cu}_2\text{Se}$  at 78 K, showing 1D moiré patterns with periodicity around 3 nm.  $V_s = -1$  V,  $I_t = 0.1$  nA. b) Atomic-resolution STM image of  $\text{Cu}_2\text{Se}$  at 78 K.  $V_s = -0.5$  V,  $I_t = 0.5$  nA. An atomic model and the corresponding STM simulation are overlaid. c) FFT of (b), revealing a twofold rotational symmetry and a rectangular unit cell. The satellite spots pointed at by blue arrows correspond to the 1D moiré pattern. d) A  $\zeta$ -phase atomic model and the unit cell (black dashed rectangle,  $a = 0.41$  nm,  $b = 0.67$  nm). The Se atoms in the middle of the rectangular unit cells cause weakening of some diffraction spots in (c). e) STM image of  $\text{Cu}_2\text{Se}$  at 300 K showing homogeneity.  $V_s = -1$  V,  $I_t = 0.1$  nA. f) Atomic-resolution STM image of  $\text{Cu}_2\text{Se}$  at 300 K.  $V_s = -0.5$  V,  $I_t = 0.5$  nA, overlaid at the bottom with an atomic model and the corresponding STM image simulation. The dashed lines in (b) and (f) indicate the position of the STM bright spots, i.e., the position of the top-layer Se atoms, and the red polyline is used to show the displacement of some top-layer Se atoms. g) FFT of (f) showing a hexagonal unit cell. h) A  $\lambda$ -phase atomic model. The  $\lambda$ -phase has the rectangular unit cell (black dashed rectangles in (f) and (h),  $a' = 0.40$  nm,  $b'' = 0.69$  nm) and has a hexagonal primitive unit cell (blue dashed rhombuses in (f) and (h),  $a' = b' = 0.40$  nm). Comparing with the lattice parameter of the  $\zeta$ -phase, the lattice parameter of the rectangular unit cell  $a$  ( $a'$ ) decreases, while  $b$  ( $b''$ ) increases. Freestanding monolayers are used for STM simulations as the interaction between  $\text{Cu}_2\text{Se}$  monolayers and graphene is weak compared with the in-plane chemical bonding.

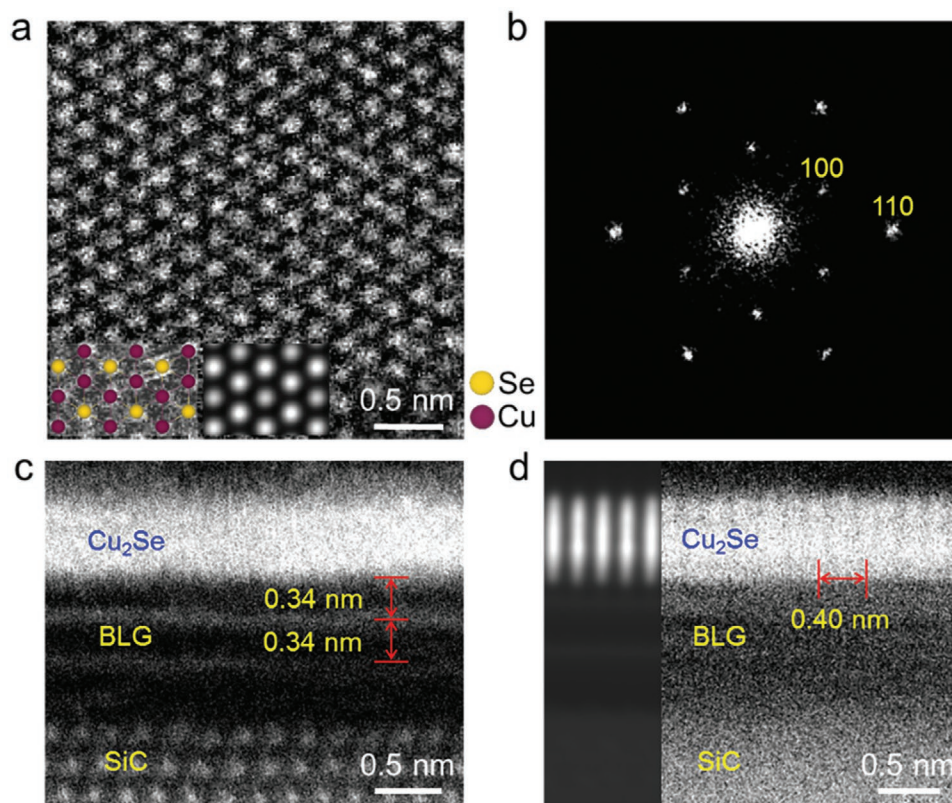


**Figure 2.** STEM images of monolayer Cu<sub>2</sub>Se at 300 K. a) Atomic-resolution plane-view image with an overlaid  $\lambda$ -phase atomic model and simulated image. b) FFT of (a), showing threefold rotational symmetry. c) Cross-sectional edge-on STEM image of  $\lambda$ -phase Cu<sub>2</sub>Se on a BLG-SiC substrate. d) Cross-sectional on-axis STEM image.

symmetry than the  $\zeta$  phase. The cross-sectional STEM image in Figure 2c shows a layer thickness of  $\approx 0.38$  nm, which is the same as the theoretical thickness of monolayer Cu<sub>2</sub>Se (Figure S4b, Supporting Information), confirming the sample's monolayer form. We note that the atomic columns in the cross-sectional view of Figure 2d are straight, compared with the  $\zeta$ -phase zigzag pattern shown in Figure 1d.

Retrieving information from the STM and STEM images, we constructed the atomic model shown in Figure 1h for the  $\lambda$  phase. Comparing to the atomic arrangement in the  $\zeta$  phase, the six atoms in each column are well aligned. This structure has the space group  $P\bar{3}m1$ . The DFT-relaxed lattice constants are  $a' = b' = 0.40$  nm, in excellent agreement with the experimental values  $a' = b' = 0.40 \pm 0.05$  nm. The atomic model and the corresponding simulated STM and plane-view STEM images are overlaid on Figures 1f and 2a, respectively, showing excellent agreement and thus confirming the  $\lambda$ -phase structure. We note that the  $\lambda$  phase has never been reported either as a theoretical prediction or experimental observation.

The measured distance between monolayer  $\lambda$ -Cu<sub>2</sub>Se and the graphene substrate is  $\approx 0.34$  nm (Figure 2c). The DFT-calculated value for this distance, 0.33 nm (Figure S4, Supporting Information), is in excellent agreement. Electron localization function (ELF) plots, shown in Figure S4 (Supporting Information), reveal weak, van der Waals interactions between the  $\lambda$ -Cu<sub>2</sub>Se monolayer and BLG. These interactions have minimal effect on the structure of the two phases and hence on the

phase transition, which is driven entirely by in-plane chemical-bonding rearrangements. We conclude that the phase transition is an intrinsic property of monolayer Cu<sub>2</sub>Se.

In order to explore the origins of the phase transition, we compared the total energies and performed phonon calculations for both the  $\lambda$  and  $\zeta$  structures at  $T = 0$  K. The total energy of the  $\zeta$  structure is 34 meV per formula unit lower than that of the  $\lambda$  structure. We found that the  $\zeta$  structure has no imaginary-frequency phonon modes (Figure S5a, Supporting Information), i.e., it is stable at low temperatures, while the  $\lambda$  structure has an imaginary-frequency phonon branch (Figure S5b, Supporting Information). We examined this mode's atomic displacements and found them to be precisely those that drive the linear chains into a zig-zag pattern (see Figure S5, Supporting Information). We repeated the phonon calculations at 300 K for the  $\lambda$  structure and found that there are no imaginary-frequency modes, i.e., the structure is stable at room temperatures. We also ran quantum molecular dynamics simulations at 500 K using the lattice constant of the  $\lambda$  structure (Figure S5d, Supporting Information), but placed the Cu atoms in zig-zag chains as in the  $\zeta$ -structure. The zig-zag chains quickly straighten out as in the  $\lambda$  structure, fully confirming the mechanism and pathway for the observed thermal phase transition. Both structures have the same rectangular unit cell (the  $\lambda$  phase has a hexagonal primitive unit cell) as shown in Figure 1d,h. During the  $\zeta \rightarrow \lambda$  phase transition, the lattice parameter  $a$  decreases, while  $b$  increases. When

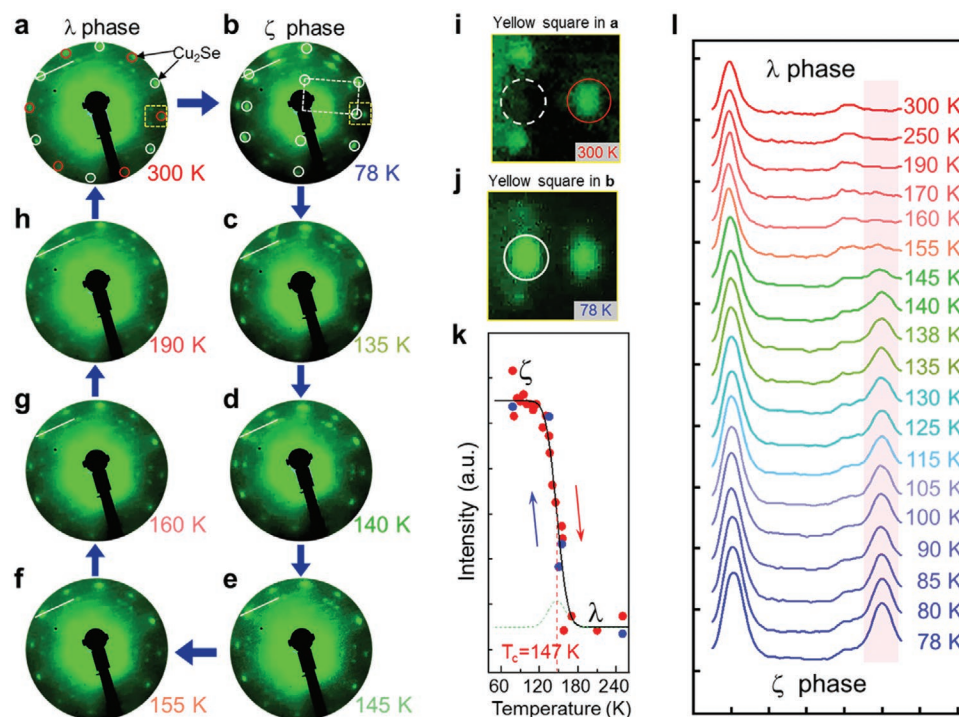


**Figure 3.** LEED patterns of monolayer  $\text{Cu}_2\text{Se}$  at different temperatures. a–h) Evolution of the monolayer  $\text{Cu}_2\text{Se}$  structure in  $k$ -space. Two sets of diffraction spots from two  $\lambda$ - $\text{Cu}_2\text{Se}$  domains rotated by  $30^\circ$  are marked by white and red solid circles while one set of diffraction spots from one  $\zeta$ - $\text{Cu}_2\text{Se}$  domain is marked by white dashed circles. See Figure S6 (Supporting Information) for details. i, j) Zoomed-in images from the yellow squares in (a) and (b), respectively. k) Temperature-dependent intensities of the diffraction spots indicated by white dashed circles in (j). Red and blue spots indicating the heating and cooling processes, respectively. The curve is fitted by cumulative distribution function of normal distribution. The transition temperature is  $\approx 147$  K. l) Evolution of the intensities of spots from the white line profile in LEED patterns in (a)–(h). The peaks, originating from the diffraction spots which are characteristic of the  $\zeta$ -phase, are highlighted by the pink window (all LEED patterns used in this figure are provided in Figure S7, Supporting Information).

$b = \sqrt{3}a$ , the  $\lambda$  phase is formed with higher symmetry and the primitive unit cell changes from rectangle to hexagon. On the other hand, the  $\zeta$  phase structure could be considered as a distorted  $\lambda$  phase structure. The displacement of some top-layer Se atoms is indicated by the red polyline connecting Figure 1b,f.

In situ, variable-temperature, LEED data shown in **Figure 3** and Figure S7 (Supporting Information) allow us to determine the phase-transition temperature. At 300 K, we see two similar sets of hexagonal diffraction spots separated by  $30^\circ$ , marked by white and red solid circles (Figure 3a). The two sets evolve similarly with temperature and can, therefore, be attributed as two sets of  $\lambda$ -phase domains (see Figure S6, Supporting Information, for details), as already inferred from STM, STEM, and DFT studies. For clarity, we monitor the evolution of only the spots marked by white circles. At  $T = 78$  K, these spots evolve into a rectangular pattern marked by white dashed circles (Figure 3b), shown clearly in the zoomed-in Figure 3i,j. The emergence of new diffraction spots as shown in the white dashed circle in Figure 3j demonstrates the presence of the  $\zeta$ -phase structure. Raising the temperature from 78 K back to 300 K, Figure 3c–h shows that the rectangular pattern fades away and the hexagonal patterns reemerge, demonstrating that the structural phase transition is purely thermal and reversible.

The intensities of the LEED spots are plotted in Figure 3k against the sample temperature. The fitting curve reveals that

the  $\text{Cu}_2\text{Se}$   $\zeta$ -to- $\lambda$  phase transition is reversible and the critical temperature is around 147 K. The temperature-dependent intensity of the diffraction peaks across the white-line profile in LEED images (Figure 3a–h) is shown in Figure 3l. The peaks highlighted in pink decrease as the temperature increases, which more directly exhibits the evolution of the new spots. The fact that each phase is stable over a fairly wide temperature range above and below a transition temperature, respectively (Figure 3) indicates that there is a phase transition rather than a crossover in monolayer  $\text{Cu}_2\text{Se}$ .

We measured the energy band structures of monolayer  $\text{Cu}_2\text{Se}$  by in situ ARPES at 78 and 300 K. **Figure 4a,b** shows the overall and second-derivative spectra for  $\zeta$ -phase monolayer  $\text{Cu}_2\text{Se}$  at 78 K, respectively. There are three equivalent domains rotated by  $120^\circ$  due to the symmetry mismatch between the sample and the substrate. All domains contribute to the ARPES data. The DFT-calculated band structures along  $\Gamma$ –Y (black) and  $\Gamma$ –P/P' (red) directions coming from different domains for the  $\zeta$ - $\text{Cu}_2\text{Se}$  phase are shown in Figure 4c and overlaid on Figure 4b. The agreement between the ARPES data and the calculated energy bands is excellent.

Figure 4e,f shows the ARPES results at 300 K and their second-derivative spectra, respectively. At the  $\Gamma$  point near the Fermi level, the split bands at 78 K change to degenerate bands at 300 K (Figure 4e), which suggests a higher symmetry at higher temperatures. Figure 4g shows the calculated energy bands of

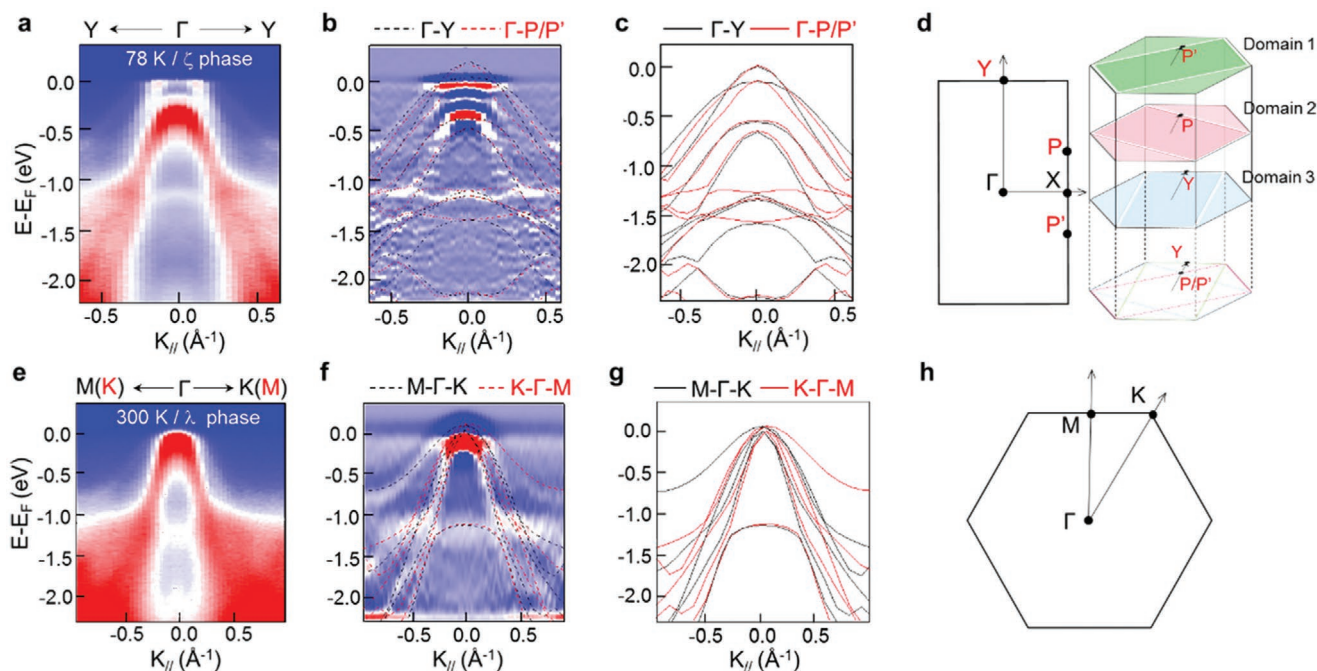


**Figure 4.** Band structures from ARPES and DFT calculations. a) Overall band structure measured along the  $\Gamma$ -Y direction at 78 K. b) Second-derivative spectra of (a) to enhance the low-density features. The overlaid black dashed lines are the calculated band structure along the  $\Gamma$ -Y direction while the red ones are along  $\Gamma$ -P/P'. c) Calculated band structure along the  $\Gamma$ -Y (black) and  $\Gamma$ -P/P' (red) directions, respectively. d) Brillouin zone of  $\zeta$ -Cu<sub>2</sub>Se.  $\Gamma$ , Y, and P/P' are labeled by black dots. e) Overall band structure measured along the M- $\Gamma$ -K directions at 300 K. f) Second-derivative spectra of (e). The overlaid black and red dashed lines are the calculated band structures along the M- $\Gamma$ -K and K- $\Gamma$ -M directions, respectively. g) Calculated band structure along the M- $\Gamma$ -K (black) and K- $\Gamma$ -M (red) directions, respectively. h) Brillouin zone of  $\lambda$ -Cu<sub>2</sub>Se (see Figure S8, Supporting Information, for details).

the  $\lambda$ -phase Cu<sub>2</sub>Se along the M- $\Gamma$ -K (black) and the K- $\Gamma$ -M (red) directions, originating from different domains. The theoretical bands are overlaid on the ARPES data in Figure 4f, showing excellent agreement. This agreement further confirms the structure of the  $\lambda/\zeta$  phases and the homogeneity of the samples. In addition, the micrometer-scale homogeneity seen in Figure S2 (Supporting Information) is sufficient to allow the collection of images such as those in Figure 1. The discontinuities seen in Figure S2 (Supporting Information), however, compromise the homogeneity at the millimeter scale of LEED and ARPES, possibly giving rise to the background in the LEED images.

Calculated band structures in multiple directions of  $\zeta$ -Cu<sub>2</sub>Se and  $\lambda$ -Cu<sub>2</sub>Se are provided in Figure S9 (Supporting Information). Even though bulk Cu<sub>2</sub>Se is metallic,<sup>[25]</sup> both the  $\zeta$  and  $\lambda$  monolayer phases are semiconducting.  $\zeta$ -Cu<sub>2</sub>Se has an indirect bandgap of 1.23 eV, while  $\lambda$ -Cu<sub>2</sub>Se has a direct bandgap of 1.30 eV. Since both Cu<sub>2</sub>Se phases below and above the transition temperature  $\approx 147$  K are semiconductors with bandgaps larger than 1.2 eV, the observed transition is not a charge-density-wave (CDW) transition.

In conclusion, we have demonstrated a purely thermal structural phase transition in a novel monolayer material. We studied the atomic and electronic structures of monolayer  $\lambda$  and  $\zeta$  phases of Cu<sub>2</sub>Se, and, based on temperature-dependent  $k$ -space structure observations, the phase transition is proved to be reversible and occurs over the entire sample. Furthermore, Cu<sub>2</sub>Se monolayers are proved to be stable in air (Figure S11a,b, Supporting Information). This purely thermal structure phase

transition in monolayer 2D material presents a potential for using monolayers in applications that exploit thermal phase transitions in bulk materials, e.g., temperature sensors.

## Supporting Information

Supporting Information is available from the Wiley Online Library or from the author.

## Acknowledgements

K.Q., L.G., X.Y.C., and H.L. contributed equally to this work. This work was supported by grants from National Key Research and Development Projects of China (Nos. 2016YFA0202300, 2018YFA0305800, and 2019YFA0308500), National Natural Science Foundation of China (Nos. 61888102, 61925111, 61622116, 51872284, and 51622211), the CAS Pioneer Hundred Talents Program, the Strategic Priority Research Program of Chinese Academy of Sciences (Nos. XDB30000000 and XDB28000000), K. C. Wong Education Foundation, and the University of Chinese Academy of Sciences. Work at Vanderbilt (S.T.P., D.L.B.) was supported by U.S. Department of Energy grant DE-FG02-09ER46554 and by the McMinn Endowment. A portion of the research was performed in the CAS Key Laboratory of Vacuum Physics. Computational resources were provided by the National Supercomputing Center in Tianjin.

## Conflict of interest

The authors declare no conflict of interest.

## Keywords

2D materials, epitaxial growth, phase transitions

Received: December 18, 2019

Revised: February 9, 2020

Published online:

- [1] K. S. Novoselov, A. K. Geim, S. V. Morozov, D. Jiang, Y. Zhang, S. V. Dubonos, I. V. Grigorieva, A. A. Firsov, *Science* **2004**, *306*, 666.
- [2] N. Mounet, M. Gibertini, P. Schwaller, D. Campi, A. Merkys, A. Marrazzo, T. Sohier, I. E. Castelli, A. Cepellotti, G. Pizzi, N. Marzari, *Nat. Nanotechnol.* **2018**, *13*, 246.
- [3] K. S. Novoselov, A. Mishchenko, A. Carvalho, A. H. C. Neto, *Science* **2016**, *353*, aac9439.
- [4] H. Yang, S. W. Kim, M. Chhowalla, Y. H. Lee, *Nat. Phys.* **2017**, *13*, 931.
- [5] J. Wang, Y. Wei, H. Li, X. Huang, H. Zhang, *Sci. China: Chem.* **2018**, *61*, 1227.
- [6] D. Rhodes, D. A. Chenet, B. E. Janicek, C. Nyby, Y. Lin, W. Jin, D. Edelberg, E. Mannebach, N. Finney, A. Antony, T. Schiros, T. Klarr, A. Mazzoni, M. Chin, Y. C. Chiu, W. Zheng, Q. R. Zhang, F. Ernst, J. I. Dadap, X. Tong, J. Ma, R. Lou, S. Wang, T. Qian, H. Ding, R. M. Osgood Jr., D. W. Paley, A. M. Lindenberg, P. Y. Huang, A. N. Pasupathy, M. Dubey, J. Hone, L. Balicas, *Nano Lett.* **2017**, *17*, 1616.
- [7] S. Z. Yang, Y. Gong, P. Manchanda, Y. Y. Zhang, G. Ye, S. Chen, L. Song, S. T. Pantelides, P. M. Ajayan, M. F. Chisholm, W. Zhou, *Adv. Mater.* **2018**, *30*, 1803477.
- [8] R. Koppera, D. Voiry, S. E. Yalcin, B. Branch, G. Gupta, A. D. Mohite, M. Chhowalla, *Nat. Mater.* **2014**, *13*, 1128.
- [9] Y. Wang, J. Xiao, H. Y. Zhu, Y. Li, Y. Alsaïd, K. Y. Fong, Y. Zhou, S. Q. Wang, W. Shi, Y. Wang, A. Zettl, E. J. Reed, X. Zhang, *Nature* **2017**, *550*, 487.
- [10] F. Arnold, R.-M. Stan, S. K. Mahatha, H. E. Lund, D. Curcio, M. Dendzik, H. Bana, E. Travaglia, L. Bignardi, P. Lacovig, D. Lizzit, Z. Li, M. Bianchi, J. A. Miwa, M. Bremholm, S. Lizzit, P. Hofmann, C. E. Sanders, *2D Mater.* **2018**, *5*, 045009.
- [11] J. Zhu, Z. Wang, H. Yu, N. Li, J. Zhang, J. Meng, M. Liao, J. Zhao, X. Lu, L. Du, R. Yang, D. Shi, Y. Jiang, G. Zhang, *J. Am. Chem. Soc.* **2017**, *139*, 10216.
- [12] G. Eda, H. Yamaguchi, D. Voiry, T. Fujita, M. Chen, M. Chhowalla, *Nano Lett.* **2011**, *11*, 5111.
- [13] D. H. Keum, S. Cho, J. H. Kim, D.-H. Choe, H.-J. Sung, M. Kan, H. Kang, J.-Y. Hwang, S. W. Kim, H. Yang, K. J. Chang, Y. H. Lee, *Nat. Phys.* **2015**, *11*, 482.
- [14] D. Voiry, A. Goswami, R. Koppera, C. e Silva Cde, D. Kaplan, T. Fujita, M. Chen, T. Asefa, M. Chhowalla, *Nat. Chem.* **2015**, *7*, 45.
- [15] Z. L. Liu, B. Lei, Z. L. Zhu, L. Tao, J. Qi, D. L. Bao, X. Wu, L. Huang, Y. Y. Zhang, X. Lin, Y. L. Wang, S. X. Du, S. T. Pantelides, H. J. Gao, *Nano Lett.* **2019**, *19*, 4897.
- [16] S. Cho, S. Kim, J. H. Kim, J. Zhao, J. Seok, D. H. Keum, J. Baik, D. H. Choe, K. J. Chang, K. Suenaga, S. W. Kim, Y. H. Lee, H. Yang, *Science* **2015**, *349*, 625.
- [17] Y. C. Lin, D. O. Dumcenccon, Y. S. Huang, K. Suenaga, *Nat. Nanotechnol.* **2014**, *9*, 391.
- [18] X. Lin, J. C. Lu, Y. Shao, Y. Y. Zhang, X. Wu, J. B. Pan, L. Gao, S. Y. Zhu, K. Qian, Y. F. Zhang, D. L. Bao, L. F. Li, Y. Q. Wang, Z. L. Liu, J. T. Sun, T. Lei, C. Liu, J. O. Wang, K. Ibrahim, D. N. Leonard, W. Zhou, H. M. Guo, Y. L. Wang, S. X. Du, S. T. Pantelides, H. J. Gao, *Nat. Mater.* **2017**, *16*, 717.
- [19] L. W. Bruch, R. D. Diehl, J. A. Venables, *Rev. Mod. Phys.* **2007**, *79*, 1381.
- [20] R. X. Fei, W. Kang, L. Yang, *Phys. Rev. Lett.* **2016**, *117*, 097601.
- [21] J. Liu, S. T. Pantelides, *Appl. Phys. Express* **2018**, *11*, 101301.
- [22] S. C. Riha, D. C. Johnson, A. L. Prieto, *J. Am. Chem. Soc.* **2011**, *133*, 1383.
- [23] M. C. Nguyen, J. H. Choi, X. Zhao, C. Z. Wang, Z. Zhang, K. M. Ho, *Phys. Rev. Lett.* **2013**, *111*, 165502.
- [24] H. Chi, H. Kim, J. C. Thomas, G. Shi, K. Sun, M. Abeykoon, E. S. Bozin, X. Shi, Q. Li, X. Shi, E. Kioupakis, A. Van der Ven, M. Kaviani, C. Uher, *Phys. Rev. B* **2014**, *89*, 195209.
- [25] D. Byeon, R. Sobota, K. Delime-Codrin, S. Choi, K. Hirata, M. Adachi, M. Kiyama, T. Matsuura, Y. Yamamoto, M. Matsunami, T. Takeuchi, *Nat. Commun.* **2019**, *10*, 72.

# ADVANCED MATERIALS

## Supporting Information

for *Adv. Mater.*, DOI: 10.1002/adma.201908314

### Air-Stable Monolayer Cu<sub>2</sub>Se Exhibits a Purely Thermal Structural Phase Transition

*Kai Qian, Lei Gao, Xiya Chen, Hang Li, Shuai Zhang, Xian-Li Zhang, Shiyu Zhu, Jiahao Yan, Deliang Bao, Lu Cao, Jin-An Shi, Jianchen Lu, Chen Liu, Jiaou Wang, Tian Qian, Hong Ding, Lin Gu, Wu Zhou, Yu-Yang Zhang, Xiao Lin,\* Shixuan Du,\* Min Ouyang, Sokrates T. Pantelides, and Hong-Jun Gao*

((Supporting Information can be included here using this template))

Copyright WILEY-VCH Verlag GmbH & Co. KGaA, 69469 Weinheim, Germany, 2020.

## Supporting Information

### **Air-Stable Monolayer Cu<sub>2</sub>Se Exhibits a Purely Thermal Structural Phase Transition**

*Kai Qian, Lei Gao, Xiya Chen, Hang Li, Shuai Zhang, Xian-Li Zhang, Shiyu Zhu, Jiahao Yan, Deliang Bao, Lu Cao, Jin-An. Shi, Jianchen Lu, Chen Liu, Jiaou Wang, Tian Qian, Hong Ding, Lin Gu, Wu Zhou, Yu-Yang Zhang, Xiao Lin\*, Shixuan Du\*, Min Ouyang, Sokrates T. Pantelides, and Hong-Jun Gao\**

#### **Methods**

**Preparation of monolayer Cu<sub>2</sub>Se on bilayer graphene on 6H-SiC(0001).** Monolayer Cu<sub>2</sub>Se was fabricated in a commercial UHV system (Omicron) with standard molecular beam epitaxy (MBE) chamber. The system operates with base pressure better than  $1 \times 10^{-10}$  mbar. Bilayer graphene (BLG) was grown on a nitrogen-doped 6H-SiC(0001) substrate by cycles of flash annealing. The BLG quality and cleanliness were verified by STM scanning and LEED. Single-layered Cu<sub>2</sub>Se was obtained by Cu (99.99%, ESPI) and Se (99.99%, Sigma-Aldrich) co-deposition from an e-beam cell (Omicron) and a standard Knudsen cell, respectively. The substrate was held at 400 K during growth while post-growth annealing was done at 500 K. After preparation, the sample was transferred to an STM chamber and scanned at  $\sim 78$  K and  $\sim 300$  K.

#### ***Ex situ* STEM characterization of single-layered Cu<sub>2</sub>Se.**

*Cross-sectional STEM sample preparation.* A graphite flake of  $\sim 50$  nm in thickness was placed on the surface of the sample [Cu<sub>2</sub>Se monolayer on BLG on 6H-SiC(0001)] as a protection layer. The TEM cross-sectional sample was then prepared using a focused-ion beam. STEM Z-contrast imaging was performed on an aberration-corrected JEOL JEM-ARM200F microscope operated at 200 kV. The convergence semi-angle was about 25 mrad and the corresponding collection angle was from 40 to 160 mrad.

*Plane-view STEM sample preparation.* Monolayer graphene was transferred to a Au quantifoil grid, which was then put into the MBE chamber and degassed at 400°C for 10 hours. Monolayer Cu<sub>2</sub>Se was grown on the graphene on the Au grid under the same conditions as on BLG. The TEM sample was baked at 160°C for 8 hours under vacuum before the microscopy experiment. STEM Z-contrast imaging was performed on an aberration-corrected Nion U-HERMES100 operating at 60 kV. The convergence semi-angle for the incident probe was 32 mrad. The image was collected for a half-angle range of  $\sim 75$  to  $\sim 210$  mrad.

STEM-ADF image simulations were performed using the QSTEM package. The plane-view

HAADF image simulation was done using the same parameters as in the experiment. The cross-sectional HAADF image simulation was done without probe aberration but with a source size of 0.6 Å for compensation.

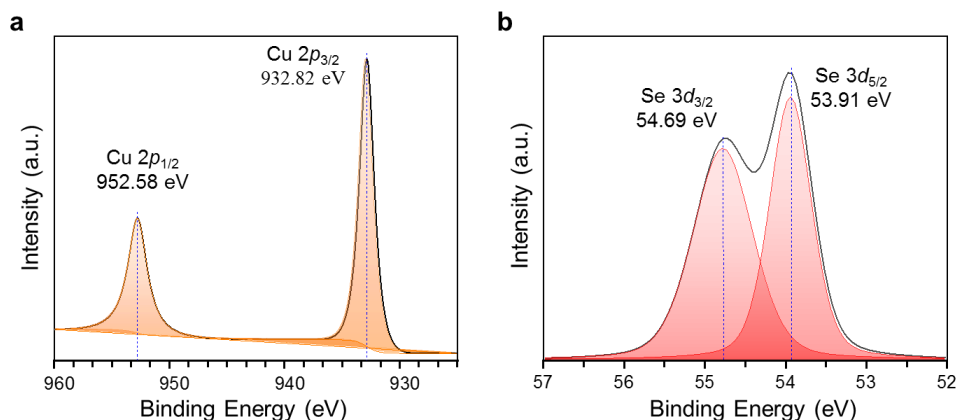
**LEED characterization of monolayer Cu<sub>2</sub>Se on BLG on 6H-SiC(0001).** Experiments were carried out with a commercial high-resolution LEED instrument (OCI). The chamber operated with base pressure better than  $1 \times 10^{-10}$  mbar. Typical emission currents were in the range of 1–5 nA; beam energies were between 0 and 120 eV. The sample in the chamber was cooled by liquid nitrogen and the temperature was monitored by thermocouples (platinum 100/250) in real time. The heating and cooling rate was 2.5 K/min.

**LEED data analysis (Curve fitting).** Intensities of Cu<sub>2</sub>Se spots are sampled from the brightness channel of LEED images in Hue-Saturation-Brightness (HSB) color space, and normalized with that of temperature-independent spots and background. The intensity-temperature black curve [Fig. 3(k)] is fitted by a cumulative distribution function of normal distribution:  $I(T) = \frac{I_m}{2} \left[ 1 - \operatorname{erf} \left( \frac{T-T_0}{\sigma\sqrt{2}} \right) \right] + I_0$ . Here erf is the Gauss error function,  $\sigma$  is the standard deviation,  $I_m$  and  $I_0$  are fitting parameters.

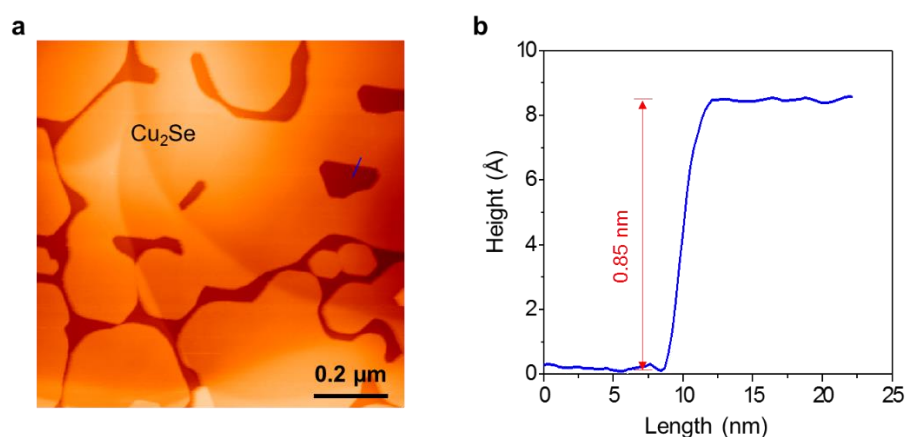
**ARPES measurements of the as-grown sample.** ARPES measurements were performed by using the He II ( $h\nu = 40.6$  eV) resonance lines and a VG SCIENTA R4000 analyzer. The angular and energy resolutions were set to  $0.2^\circ$  and 30 meV, respectively. The sample was measured at 300 K and 78 K with a working vacuum better than  $3 \times 10^{-11}$  mbar.

**XPS measurements of the as-grown sample.** *In situ* X-ray photoelectron spectroscopy measurements were performed at the Beijing Synchrotron Radiation Facility (BSRF). The sample was transferred to the XPS station by a UHV suitcase with vacuum better than  $5 \times 10^{-10}$  mbar. Monochromatic synchrotron radiation light was realized by four high-resolution gratings and controlled by a hemispherical energy analyzer that possesses a photon energy in the range from 10 to 1100 eV.

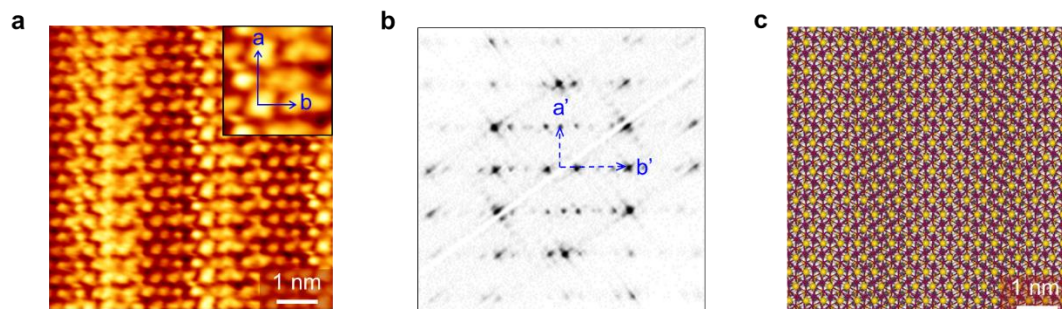
**Theoretical calculations.** Quantum mechanical calculations based on density functional theory (DFT) were performed using the Vienna ab initio simulation package (VASP)<sup>1,2</sup>. The projector augmented wave (PAW) method and the local-density approximation (LDA)<sup>3,4</sup> for the exchange-correlation functional were adopted. The rotationally invariant LDA+U formalism proposed by Dudarev et al.<sup>5</sup> was used with  $U_{\text{eff}} = 6.52$  eV for Cu<sup>6</sup>. 450 eV energy cutoff and 15 Å vacuum layers were used for structure relaxations. Total energies were converged to  $10^{-4}$  eV, and forces were converged to 0.001 eV/Å. The  $k$ -points sampling was  $39 \times 39 \times 1$  and  $27 \times 15 \times 1$  for the  $\lambda$  and  $\zeta$  phases, respectively.



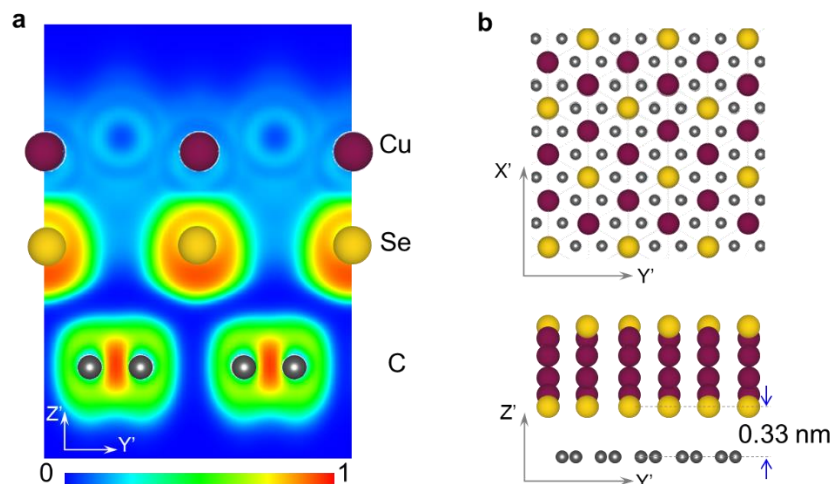
**Supplementary Figure 1: XPS characterization of monolayer  $\text{Cu}_2\text{Se}$  on BLG at 300 K.** **a**, **b** The core-level spectra of Cu and Se, respectively. All of the peaks are sharp and similar to the core levels in bulk  $\text{Cu}_2\text{Se}$ <sup>7</sup>, indicating the film is  $\text{Cu}_2\text{Se}$ .



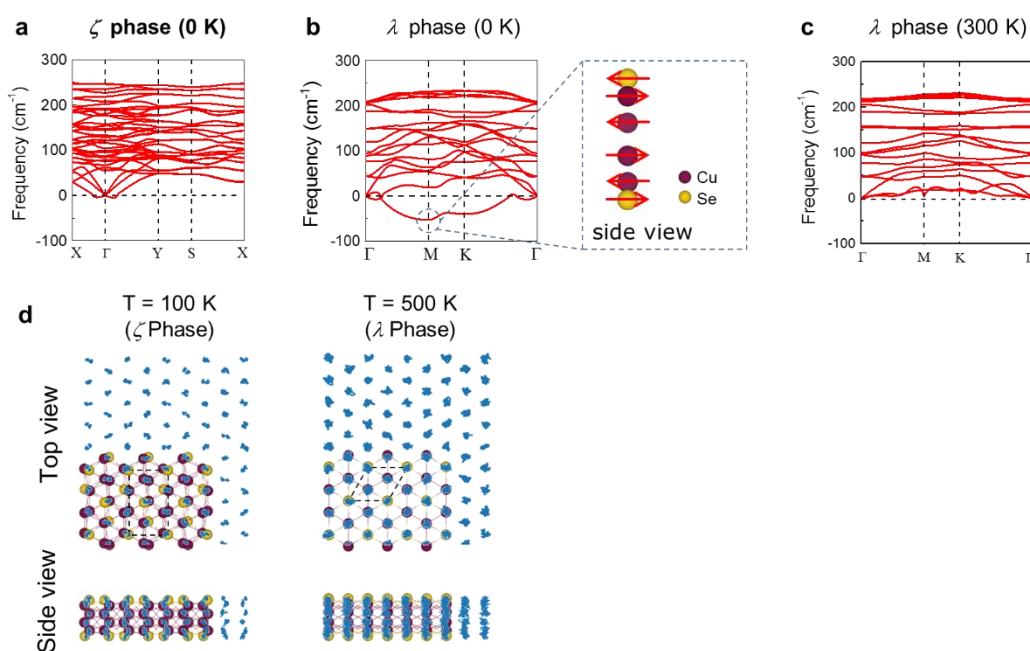
**Supplementary Figure 2: A large-scale scanning tunneling microscopy (STM) image taken on the monolayer  $\text{Cu}_2\text{Se}$  on a BLG substrate.** **a** High-quality, micron-size  $\text{Cu}_2\text{Se}$  films on BLG. **b** The line profile along the blue line in **a**, showing the height of the as-grown layer is 0.85 nm.  $V_s = -3$  V,  $I_t = 0.03$  nA.



**Supplementary Figure 3: STM image, FFT and model of  $\zeta\text{-Cu}_2\text{Se}$  on a BLG substrate.** **a** An STM image for  $\zeta\text{-Cu}_2\text{Se}$  on a BLG substrate at 78 K.  $V_s = -0.5$  V,  $I_t = 0.5$  nA. Inset shows the primitive lattice. **b** FFT of **a**. **c** Top view of a model of  $\zeta\text{-Cu}_2\text{Se}$  on a BLG substrate.

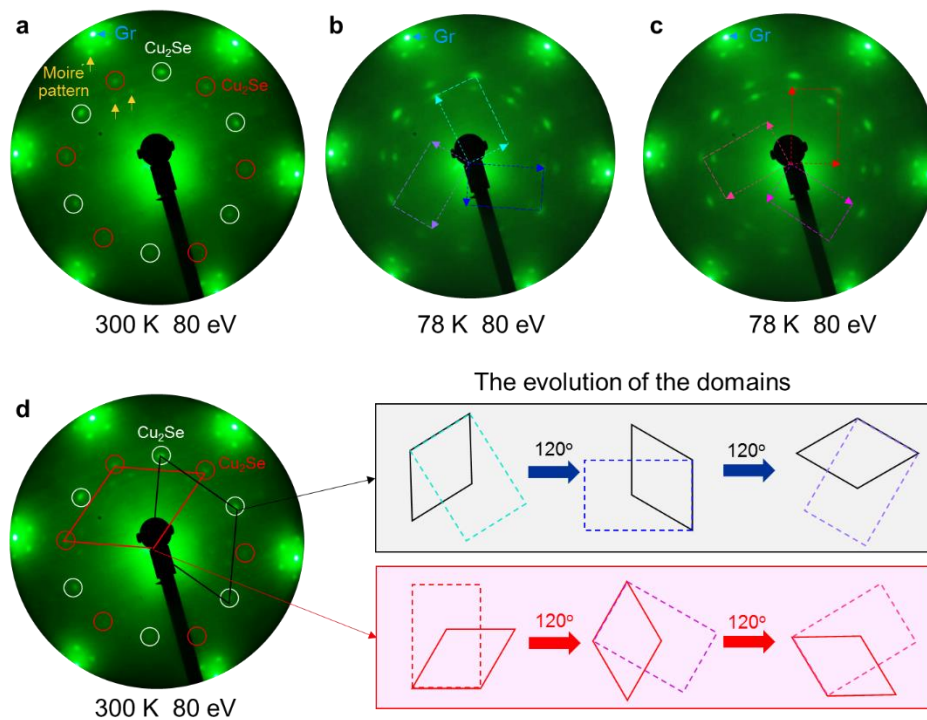


**Supplementary Figure 4: Calculated ELF and the atomic model of the  $\lambda$ -Cu<sub>2</sub>Se on graphene.** **a** Cross-sectional ELF map of the  $\lambda$ -Cu<sub>2</sub>Se on graphene. **b** Model of the  $\lambda$ -Cu<sub>2</sub>Se on graphene, both the top- and side-view images are shown.

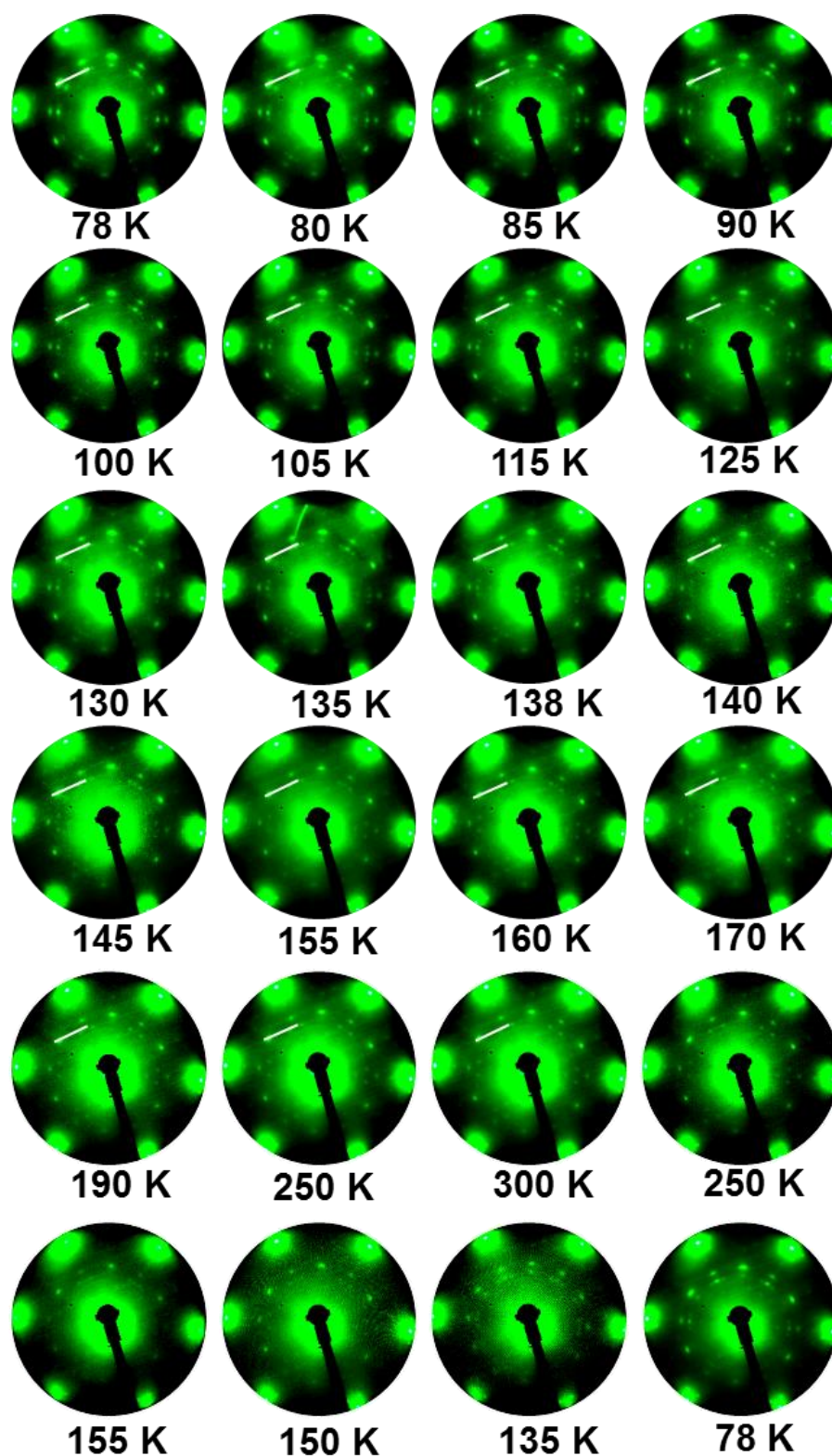


**Supplementary Figure 5: Phonon dispersion calculations of  $\zeta$ -Cu<sub>2</sub>Se and  $\lambda$ -Cu<sub>2</sub>Se.** **a, b** Phonon dispersion of  $\zeta$ -Cu<sub>2</sub>Se and  $\lambda$ -Cu<sub>2</sub>Se at 0 K, respectively. For  $\zeta$ -Cu<sub>2</sub>Se, there is no imaginary frequency except for the small ones near the  $\Gamma$  point due to numerical errors. For  $\lambda$ -Cu<sub>2</sub>Se, there are imaginary frequencies distributed in almost the whole momentum space, which indicates the ground state of Cu<sub>2</sub>Se at 0 K is  $\zeta$  phase. The vibration of the imaginary phonon mode at M point, which is related to an in-plane optical mode, is schematically shown

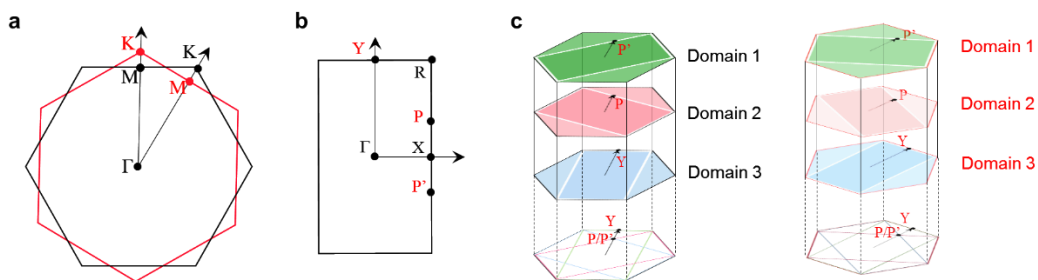
in the right panel of **b**. **c** Phonon dispersion of  $\lambda$ -Cu<sub>2</sub>Se at 300 K. The absence of imaginary modes indicates that, at 300 K,  $\lambda$ -Cu<sub>2</sub>Se is stable. The phonon dispersions in **a** and **b** are calculated using density functional perturbation theory (DFPT) as implemented in VASP. The phonon dispersions in **c** are calculated using self-consistent phonon (SCPH) theory with anharmonic effects as implemented in the ALAMODE package [8]. **d** Quantum molecular dynamics (QMD) simulations at 100 K and 500 K, using the lattice constant of the  $\lambda$  phase and the structure of the  $\zeta$  phase. At  $T = 100$  K, the Cu<sub>2</sub>Se keeps the  $\zeta$  phase structure. As we increase the temperature to 500 K, the Cu<sub>2</sub>Se transforms to the  $\lambda$  phase structure. QMD simulations were performed at  $T = 500$  K to speed up the process.



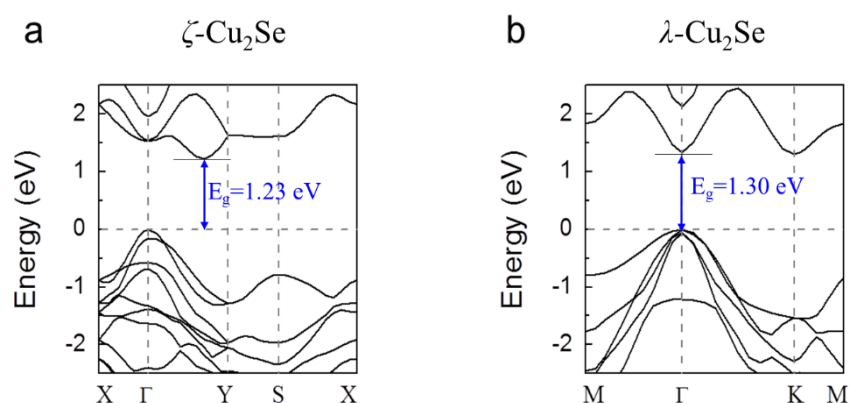
**Supplementary Figure 6: LEED patterns of monolayer Cu<sub>2</sub>Se at 300 K and 78 K. a** LEED pattern (at 80 eV) of monolayer Cu<sub>2</sub>Se on bilayer graphene on 6H-SiC(0001) at 300 K. The diffraction spots from the graphene substrate and the moiré pattern are marked by blue arrows and orange arrows, respectively<sup>8</sup>. Two sets of Cu<sub>2</sub>Se diffraction spots are pointed out by white and red solid circles. **b, c** LEED pattern (at 80 eV) of the same sample obtained at 78 K. **d** Considering the lattice mismatch between the  $\lambda/\zeta$ -Cu<sub>2</sub>Se and the substrate, the structure of the  $\lambda$ -phase Cu<sub>2</sub>Se (300 K) has three-fold rotational symmetry while the  $\zeta$ -phase (78 K) has only two-fold, which causes one set of spots at 300 K to yield three equivalent sets of spots at 78 K.



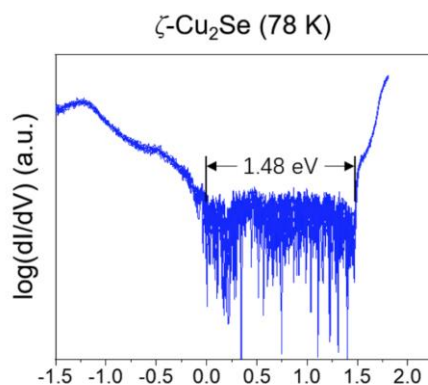
**Supplementary Figure 7: All LEED patterns used for the determination of the transition temperature of the structural phase transition.** All LEED patterns are obtained at an electron beam energy of 80 eV. The heating and cooling rate is 2.5 K/min. The white lines in every LEED image are the line profiles shown in Fig. 31.



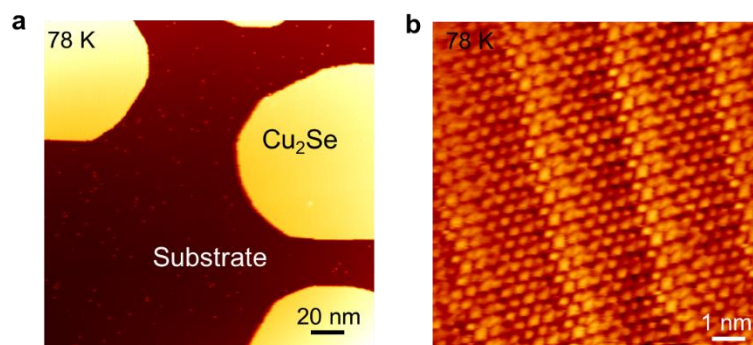
**Supplementary Figure 8: Brillouin zone of  $\text{Cu}_2\text{Se}$ .** **a** Brillouin zone of  $\lambda\text{-Cu}_2\text{Se}$ . Black and red hexagons show two domains with a rotation angle of  $30^\circ$ . **b** Brillouin zone of  $\zeta\text{-Cu}_2\text{Se}$ . **c** Each domain at 300 K gives rise to three domains at 78 K. The ARPES spectrum band dispersion along the  $\Gamma$ -Y direction contains the signals from the  $\Gamma$ -Y in one domain and the  $\Gamma$ -P and  $\Gamma$ -P' contributed from the other two domains.



**Supplementary Figure 9: Electronic band structures of  $\zeta\text{-Cu}_2\text{Se}$  and  $\lambda\text{-Cu}_2\text{Se}$  at HSE06 level.** **a, b** Electronic band structures of  $\zeta\text{-Cu}_2\text{Se}$  and  $\lambda\text{-Cu}_2\text{Se}$ , respectively. Both phases are semiconductors.



**Supplementary Figure 10: STS spectrum at 78 K of monolayer  $\text{Cu}_2\text{Se}$ .** At 78 K,  $\text{Cu}_2\text{Se}$  monolayers are  $\zeta$  phase, which is a semiconductor with a band gap  $\sim 1.48$  eV. STS spectra at RT are difficult to obtain because of thermal fluctuations.



**Supplementary Figure 11: STM images of monolayer  $\text{Cu}_2\text{Se}$  after two hours in air.** The sample was exposed in air without any protection for two hours, then taken back to the UHV chamber and annealed at 400 K to remove possible adsorbates. **a** A large-scale STM image shows monolayer  $\text{Cu}_2\text{Se}$  islands on a BLG substrate.  $V_s = -2$  V,  $I_t = 0.1$  nA. **b** A high-resolution STM image of monolayer  $\text{Cu}_2\text{Se}$  shows similar features with that in Supplementary Fig. 3a, which was kept in the UHV chamber after fabrication.  $V_s = -0.1$  V,  $I_t = 0.8$  nA.

### References

- [1] G. Kresse; J. Furthmuller, *Phys. Rev. B* **1996**, *54*, 11169-11186.
- [2] G. Kresse; J. Furthmuller, *Comput. Mater. Sci.* **1996**, *6*, 15-50.
- [3] D. M. Ceperley; B. J. Alder, *Phys. Rev. Lett* **1980**, *45*, 566-569.
- [4] J. P. Perdew, A. Zunger, *Phys. Rev. B* **1981**, *23*, 5048-5079.
- [5] S. L. Dudarev; G. A. Botton; S. Y. Savrasov; C. J. Humphreys; A. P. Sutton, *Phys. Rev. B* **1998**, *57*, 1505-1509.
- [6] D. Wu; Q. Zhang; M. Tao, *Phys. Rev. B* **2006**, *73*, 235206.
- [7] S. C. Riha; D. C. Johnson; A. L. Prieto, *J. Am. Chem. Soc.* **2011**, *133*, 1383-1390.
- [8] C. Riedl; C. Coletti; T. Iwasaki; A. A. Zakharov; U. Starke, *Phys. Rev. Lett* **2009**, *103*, 246804.